

Multifunctional Optoelectronic Device Based on an Asymmetric Active Layer Structure

Beitao Ren, Gancheong Yuen, Sunbin Deng, Le Jiang, Dingjian Zhou, Leilei Gu, Ping Xu, Meng Zhang, Zhiyong Fan, Fion Sze Yan Yueng, Rongsheng Chen, Hoi-Sing Kwok, and Guijun Li*

A single device with a variety of capabilities is highly attractive for the increasing demands of complex and multifunctional optoelectronics. A hybrid heterojunction formed between CsPbBr₃ halide perovskite and chalcogenide quantum dots is demonstrated. The heterojunction served as an asymmetric active layer allows not only charge separation/exciton dissociation in a benign process, but also carrier injection/recombination with the suppression of bulk and interfacial nonradiative recombination. An individual device incorporating such a heterojunction is therefore implemented with an integration of proof-of-concept functions, including a voltage controllable multicolor light-emitting diode, an exceptionally high photovoltage energy-harvesting device, and an ultrafast photosensitive detector. The figures of merit of the light-emitting diode remarkably surpass those of the corresponding single-active-layer device, particularly in terms of its bright electroluminescence and superior long-term stability. The asymmetric active layer concept provides a feasible route to design efficient multifunctional and monofunctional devices in the future.

1. Introduction

As monofunctional devices mature and approach their fundamental limits, a pivotal question now is how to develop technologies enabled with increasing functionality and reduced

product size. Putting together miniaturized devices with a variety of capabilities in tight spaces is a typical approach.^[1] For example, wearables, such as smart-watches, heads-up displays, powering batteries, sensors, and so on, can be enabled with full functionality and portability in a smaller footprint via device integration/miniaturization.

The monolithic integration of two or three of the optoelectronic components into a chip/system can advance inspiring and promising applications. For example, on-chip integration of transistor, light emitters, and photodiodes opens an avenue for developing a variety of applications, such as smart lighting, on-chip optical interconnect, optical wireless communication, and optoisolators.^[2–4] Organic light emitting diodes (OLEDs) integrated with photovoltaic device in a tandem structure provides a new application of

portable display and ecofriendly devices.^[5,6] Although the pursuit of optoelectronic integration leads to an increase in device functionality and an improvement in performance, the manufacturing for a series of monofunctional components and then integrating them into a system will definitely increase fabrication complexity as well as product costs.^[7] Therefore, to achieve an individual component that equipped with multiple functions is highly desirable, which can simplify the fabrication process, reduce manufacturing costs, boost the integration level, and expand possible application fields.

Although optoelectronic devices share almost the same material requirements of high carrier lifetime, long diffusion length, tolerance to defect density, and low nonrecombination,^[8,9] the task of to endow multifunctionality within a single-device structure has always been challenging. In optoelectronic devices, the processes of sourcing and detecting light are converse. The charge extraction and charge injection take place at the same interface. For example, a solar cell converting light into electricity requires efficient carrier separation and collection,^[10] while a light-emitting diode (LED) prefers energetic carrier injection and radiative recombination.^[11] It is difficult for the conventional design for the device with a single active layer to achieve efficient charge extraction and charge injection simultaneously, as the structure is presupposed to facilitate only one directional transport. In order to realize independent


B. Ren, G. Yuen, L. Jiang, D. Zhou, Prof. P. Xu, Prof. M. Zhang, Prof. G. Li

College of Electronic Science and Technology
Shenzhen University
Shenzhen 518060, P. R. China
E-mail: gliad@connect.ust.hk

S. Deng, Dr. F. S. Y. Yueng, Prof. H.-S. Kwok
State Key Lab of Advanced Displays and Optoelectronics Technologies
Hong Kong University of Science and Technology
Clear Water Bay, Kowloon, Hong Kong

Dr. L. Gu, Prof. Z. Fan
Department of Electronic and Computer Engineering
The Hong Kong University of Science and Technology
Clear Water Bay, Kowloon, Hong Kong

Prof. R. Chen
School of Electronic and Information Engineering
South China University of Technology
Guangzhou 510640, P. R. China

 The ORCID identification number(s) for the author(s) of this article can be found under <https://doi.org/10.1002/adfm.201807894>.

DOI: 10.1002/adfm.201807894

control over the carrier injection and extraction processes, the device should incorporate the active layer with an asymmetric energy band structure. Using the heterojunction, which is formed between any two semiconductors, is the approach that first comes to mind in addressing the above issues. However, previous attempts to use of the heterojunction have mainly focused on either improving charge extraction in solar cells or enhancing radiative recombination in LEDs.^[12] Most recently, Oh et al. reported double-heterojunction nanorods containing a type I straddling band offset and a type II staggered band offset.^[13] Their device structure endows the device with the capacity to be as a dual-functioning display.

The recent development of halide perovskite and colloidal quantum dots opens feasible routes to separate the charge injection and carrier extraction processes by forming a heterojunction active layer, as both materials show high quantum yield for photo- and electroluminescence and their bandgap can be continuously tuned by modifying the chemical composition and particle size.^[14–17] Here we demonstrate an individual device with a heterojunction active layer in a p–i–n configuration. The heterojunction formed between the inorganic halide perovskite (CsPbBr₃) and chalcogenide quantum dots (CdSe/ZnS QDs) enables efficient electron–hole recombination and carrier extraction under different operation conditions. As a result, the single device can operate as a voltage controllable multicolor LED, an efficient solar cell, and a sensitive photodetector. In addition, the heterojunction device is accompanied with several key advantages that outweigh the single-active-layer counterparts, including bright electroluminescence, superior long-term stability, a remarkably

high photovoltage, ultrafast on-off switching, simultaneous light detection, and light emission, etc.

2. Results and Discussion

2.1. Heterojunction Properties of CsPbBr₃/CdSe Active Layer

The device fabrication process is a combination of solution-processing and vacuum evaporation techniques (see Experimental Section). As shown in **Figure 1A**, the device is generally based on a p–i–n configuration, with the active layer sandwiched between a p-type hole transport layer (HTL) and an n-type electron transport layer (ETL) layer. The active layer is made with a CsPbBr₃/CdSe heterojunction that works as either a light emission layer or a light absorbing layer. Here the inorganic perovskite is the protonated salt of aminovaleric acid bromide (AVAB)-doped CsPbBr₃ (CsPbBr₃ hereafter) and the CdSe quantum dots are red emissive CdSe/ZnS colloidal quantum dots (CdSe hereafter). The p-type layer is magnesium-doped nickel oxide, while magnesium-doped zinc oxide serves as the n-type layer.^[18] Additionally, an ultrathin poly(4-vinylpyridine) (PVP) insulating layer between the p-type NiMgO_x and CsPbBr₃ is used to suppress interfacial nonradiative recombination.^[19] The cross-sectional scanning electron microscope (SEM) image in **Figure 1B** shows that the CsPbBr₃ and CdSe have a thickness of 90 nm and 20–30 nm, respectively.

The energy level of the CsPbBr₃ and CdSe was determined with ultraviolet photoelectron spectroscopy (UPS) and UV–vis

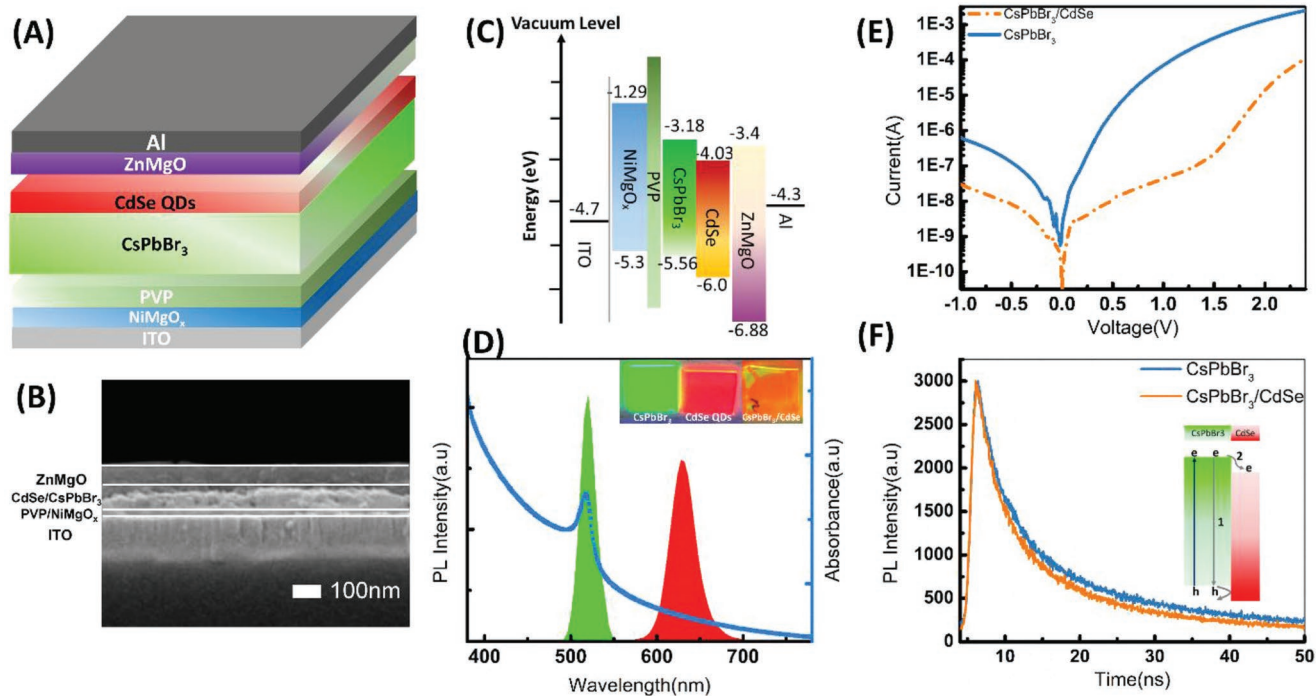


Figure 1. A) Schematic of the heterojunction device; B) cross-sectional SEM image; C) energy band structure; D) photoluminescence and absorbance of the CsPbBr₃/CdSe heterojunction. Insets are the photograph of the CsPbBr₃, CdSe, and CsPbBr₃/CdSe films under a 365 nm ultraviolet lamp; E) dark current–voltage curves of the devices with a CsPbBr₃/CdSe heterojunction active layer or a CsPbBr₃ single active layer; F) time-resolved photoluminescence of the CsPbBr₃ and CsPbBr₃/CdSe films. The excitation wavelength is 358 nm, the photoluminescence is monitored at a wavelength of 524 nm. The inset is the schematic of the electron transfer process.

absorption experiments. The valence band (VB) relative to the vacuum was measured to be -5.56 eV for CsPbBr₃ and -6.0 eV for CdSe, for which the conduction band (CB) is determined to be -3.18 and -4.03 eV, respectively (Figure S1, Supporting Information). Figure 1C presents the schematic of the energy level diagram of our heterojunction device. When CsPbBr₃ and CdSe are stacked together, they form a type II heterojunction with an anisotropic staggered offset, which has been shown to allow efficient photoinduced charge separation^[20,21] and improved light amplification.^[22] Meanwhile, CsPbBr₃ shows a prominent excitonic absorption edge near 2.38 eV (Figure 1D). The excitonic absorption feature suggests good luminescent properties of the AVAB-doped CsPbBr₃, as can be seen from the bright green emission of the CsPbBr₃ film under a 365 nm ultraviolet lamp. When stacked with CdSe, the hybrid film looks orange, which is the result of the color mixing of green (CsPbBr₃) and red (CdSe) emission. The corresponding hybrid film exhibits two photoluminescence (PL) peaks featured at 520 and 628 nm (Figure 1D), resulting from the photoemission of CsPbBr₃ and CdSe, respectively.

The electrical properties of the diodes were characterized by the current (I)–voltage (V) measurement under dark conditions. The device with a CsPbBr₃ single active layer is given as a reference. As shown in Figure 1E, both of the devices demonstrate a good diode-rectifying behavior. As estimated from the two-diode model fitting of the dark IV ,^[23] the heterojunction device exhibits a four orders lower recombination ($j_{02} = 7.3 \times 10^{-11}$ mA cm⁻²) than that of the device with a CsPbBr₃ single layer ($j_{02} = 4.7 \times 10^{-7}$ mA cm⁻²). The details of the simulation data and experimental data are provided in Figure S2 (Supporting Information). The reduced recombination for the heterojunction device compared with the CsPbBr₃ device is reasonably attributed to the interface modification by the introduction of the additional CdSe layer. The interface modification was further confirmed by the measurement of the PL intensity and lifetime. As shown in Figure S3 (Supporting Information), both of the PL intensity and lifetime largely increase when CdSe is inserted between the CsPbBr₃ and ZnMgO. As the quantum dots are capped with organic ligands, the deposition of the CdSe on the top of CsPbBr₃ can passivate the surface defects, which is also implied by the narrow bandwidth electroluminescence spectrum of the heterojunction device (18.8 nm) compared with that of the CsPbBr₃ device (20.4 nm). Indeed, the CsPbBr₃/Zn(Mg)O interface represents one of the decay pathways for the carrier.^[24,25] In comparison, the CdSe/Zn(Mg)O interface has been demonstrated to facilitate the interfacial charge-transfer processes, which are responsible for both injecting/extracting electrons and enhancing the emission performance and stability of emitters.^[26]

To shed light on the carrier transfer behavior at the CsPbBr₃/CdSe interface, time-resolved photoluminescence (TRPL) was used to characterize the photoluminescence decay via a time-correlated single photon counting (TCSPC) system. A comparison of the photoluminescence intensity decay as a function of time for the CsPbBr₃ and CdSe/CsPbBr₃ films monitored at a wavelength of 524 nm is given in Figure 1F. The photoluminescence decay curves were fitted to a bi-exponential function with different time constants of decay (τ_1 , τ_2) in the range of a few ns. As summarized in Table 1, the CdSe/CsPbBr₃ film

Table 1. Carrier lifetimes extracted by fitting to the TRPL decay curves using a biexponential decay function. The average carrier lifetime (τ_{ave}) is calculated from the time constants τ_1 and τ_2 . a_1 and a_2 are the pre-exponential factors for τ_1 and τ_2 , respectively.

Film, monitoring wavelength	τ_1 [ns](a_1 %)	τ_2 [ns](a_2 %)	τ_{ave} [ns]
CsPbBr ₃ ,524 nm	3.24 (69.6%)	24.8 (30.4%)	9.8
CsPbBr ₃ /CdSe,524 nm	2.95 (72.3%)	21 (27.7%)	8.0
CdSe,630 nm	17.5 (90.6%)	50 (9.4%)	20.5
CsPbBr ₃ /CdSe,630 nm	16.7 (90%)	50 (10%)	20.0

has a shorter carrier lifetime (8 ns) in comparison with that of the CsPbBr₃ (9.8 ns), suggesting electron transfer (ET) from the CsPbBr₃ to CdSe in the heterojunction. The ET is primarily assisted by the 0.85 eV potential difference between the CBs of the CsPbBr₃ and CdSe. Most recently, ET from the CsPbBr₃ to CdSe has also been observed using the transient absorption and photoluminescence spectroscopies.^[27] The transfer of the electrons leaves alone the holes staying in the CsPbBr₃ due to the 0.44 eV potential barrier between the VBs of the CsPbBr₃ and CdSe (inset of Figure 1F). The charge transport behavior in CdSe is almost the same as in CsPbBr₃, where holes transfer from the CdSe to CsPbBr₃ and electrons stay in the CdSe. As the carrier lifetime in CdSe is longer (20 ns) than that in the CsPbBr₃, the transferred electrons will not disappear immediately. Instead, they will contribute to the conductivity enhancement of the CdSe or recombine with holes to generate light. Simply estimated from the difference of the PL intensity curves in Figure 1F, the potential-driven transfer process occurs 2–3 ns after the excitation, which is fast and in the time range of the carrier lifetime. In other words, the heterojunction itself provides a way for the electrons/holes to separate, and these separated electrons/holes enhance the conductivity of the heterojunction. Unlike the conventional device, this charge separation takes place within the active layer. The charge separation and charge injection are then separated independently, which is considered as key features for obtain high performance of light harvesting/detecting devices and LEDs.

2.2. Voltage Controllable Multicolor Electroluminescence

At forward bias, the device operates as a LED. As both the CsPbBr₃ and CdSe are efficient luminescence materials, electroluminescence can take place in either the CsPbBr₃ or CdSe, depending on the spatial distribution of the recombination zone. As shown in Figure 2, at a low bias, the device has a red emission at a central wavelength of 628 nm and a bandwidth of 35 nm. When the bias increases to 2.04 V, green emission appears. The green emission wavelength is centered at the 520 nm, with a bandwidth of 19 nm. The continual increase of the applied voltage is accompanied by an increase of the relative intensity of the green emission. Accordingly, the representative features of the chromaticity coordinates (CIE 1931) vary systematically from (0.6788, 0.3149) to (0.1817, 0.6873) (Figure 3A), and correspondingly, the color changes gradually from red to orange to yellow, and eventually to green (see inset of Figure 2). The photographs corresponding different applied voltages are

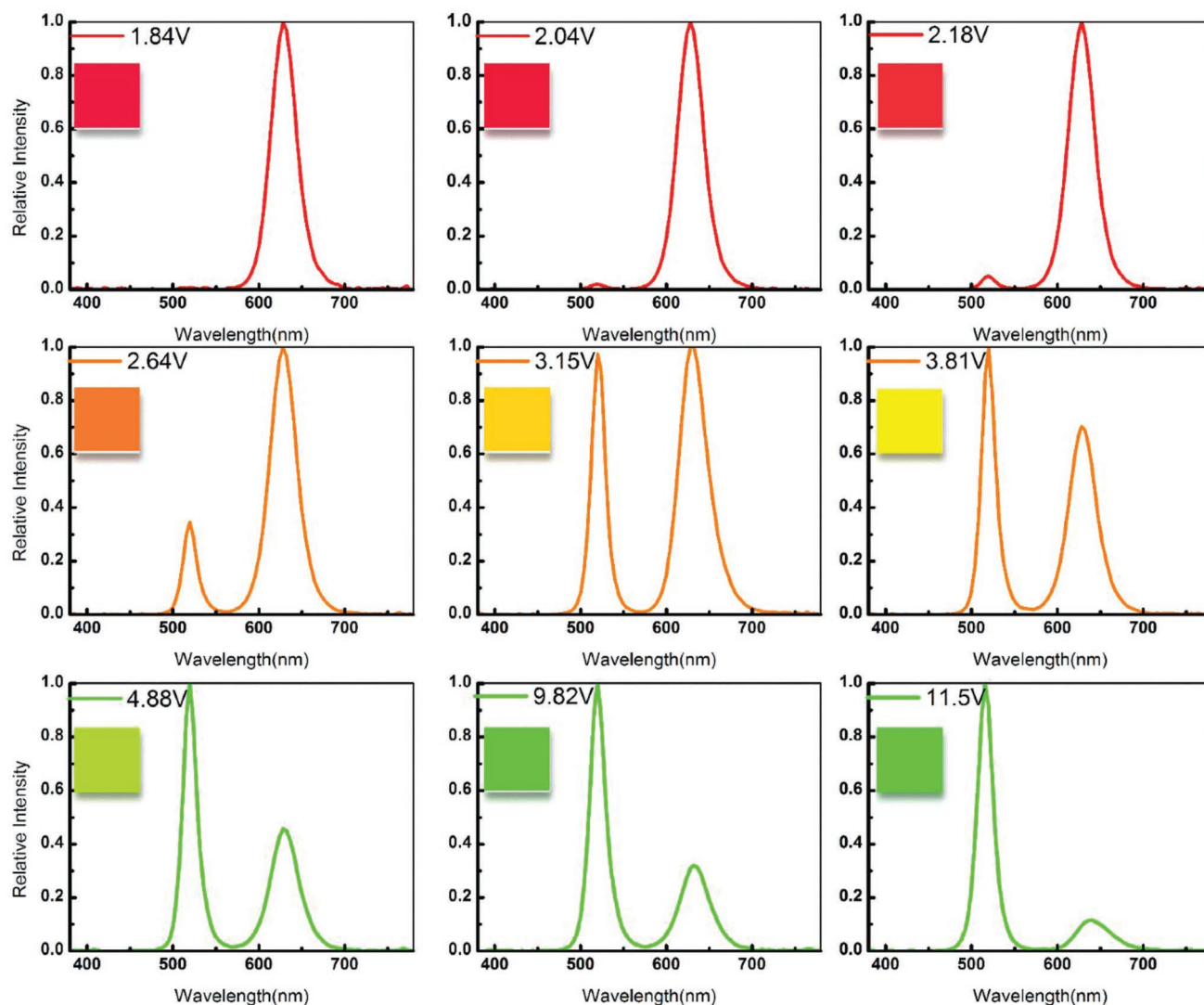


Figure 2. Voltage controllable multicolor electroluminescence. The electroluminescence spectrum is normalized to the dominated emission. The insets show the corresponding emission color. The LED was measured under constant current injection. The applied voltage showing here is related to different current density applied to the device.

given in Figure S4 (Supporting Information). A video recorded to show the voltage-controllable multicolor electroluminescence is provided in movie S1 (Supporting Information).

In order to get insight into the color-tunable property, the quantum yield of the active layers has been measured under a light intensity of $40 \mu\text{W cm}^{-2}$ (excited at 350 nm). Within the device, it was found that the quantum yield of the CsPbBr_3 (14%) is smaller than that of the CdSe (34%). Therefore, the color change cannot be simply related to the different quantum yields of perovskite and CdSe layers. The luminescence of the heterojunction device under a 385 nm excitation at different bias was further measured, as shown in Figure 3B. At zero bias, only the photoexcitation contributes to the luminescence. The green emission is weaker than the red emission, which is in good agreement with the results of the quantum yield. When a positive bias is applied and gradually increases to 3, 4, and then 5 V, the luminescence intensity of the green emission is

increased by a factor of 7, 41, and 144, respectively. In comparison, the intensity of the red emission is only increased by a factor of 1.15, 1.7, and 2.6, respectively. The significant increase of the green emission suggests that it is the electrical injection, instead of the different quantum yield of emission layers, dominating the color change of the device. The electrically induced color change from red to green is then reasonably related to the main recombination zone shifts from the CdSe to the CsPbBr_3 .

We notice that the turn-on voltages for the red (1.77 V) and green (2.0 V) emission are smaller than the bandgap voltage (the bandgap energy divided by the electron charge) of the CdSe (1.97 V) and CsPbBr_3 (2.38 V), and also lower than the turn-on voltages of the single-active-layer devices. The turn-on voltage of the CdSe LED is 1.95 V, and the turn-on voltage of the CsPbBr_3 LED is 2.26 V. The sub-bandgap turn-on voltage is possibly attributed to either the Auger-assisted charge up-conversion process occurring at the $\text{CsPbBr}_3/\text{CdSe}$ interface,^[28,29] or the

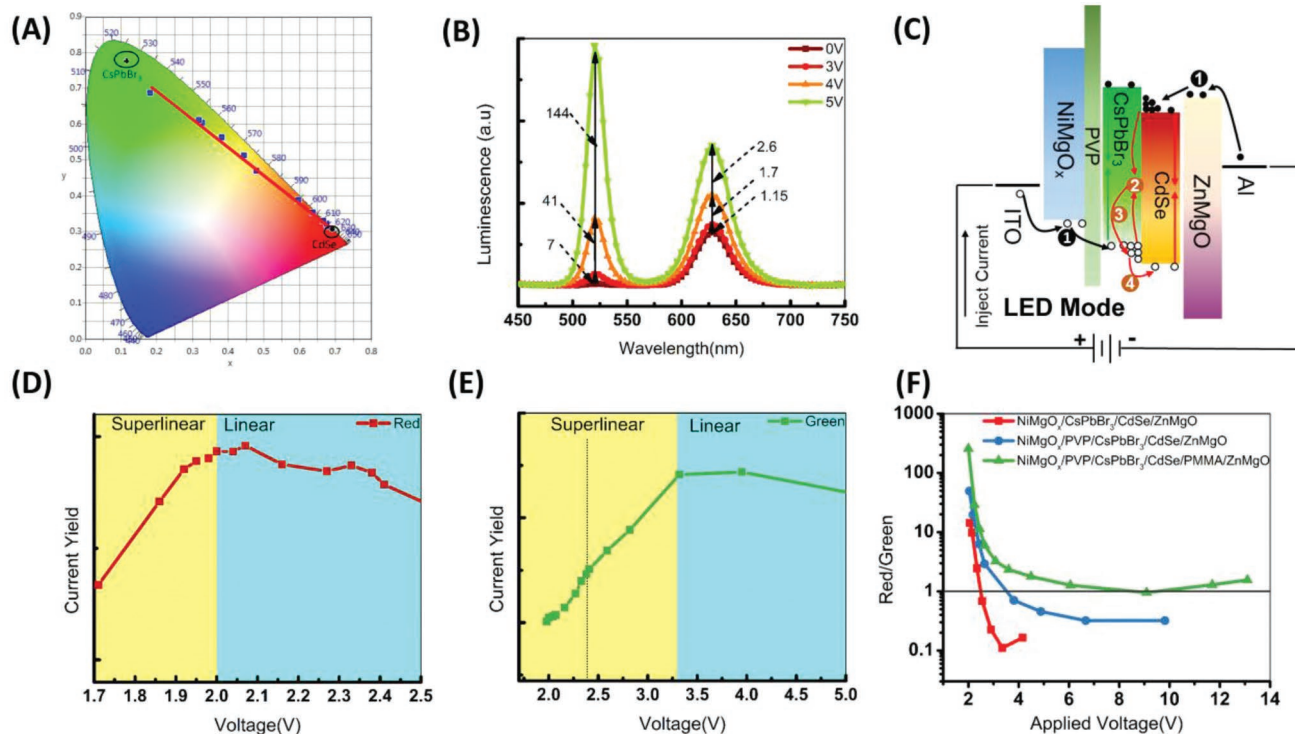


Figure 3. A) The corresponding CIE 1931 coordinates of the heterojunction device at different biases. The CIE coordinates of the CsPbBr₃ and CdSe single-active-layer devices are also provided for reference; B) the luminescence intensity of the heterojunction device as a function of the applying voltage. The device was excited by a 385 nm UV light during the measurement. C) The schematic of the device operation under forward bias. the Auger-assisted charge up-conversion process is described in steps 2, 3, and 4 (the red indicated lines); D) the current yield of the red emission as a function of the voltage; E) the current yield of the green emission as a function of the voltage; F) the red/green emission ratio of the device with different device structures.

Boltzmann distribution of the carriers that a certain number of carriers have sufficient energy to generate bandgap photons even if the voltage is slightly below the bandgap voltage. We know that the Auger-assisted process requires a high charge density. In our device, this prerequisite is fulfilled by the staggered offset between the CsPbBr₃/CdSe. The Auger process is illustrated in Figure 3C. When applying a positive voltage, holes are injected into the CsPbBr₃ from the NiMgO_x while electrons are injected into the CdSe from the ZnMgO, and then both groups move toward the CsPbBr₃/CdSe interface. Because of the band offset, holes accumulate at the interface near the side of the CsPbBr₃ and electrons accumulate at the interface near the side of the CdSe. The accumulated electrons and holes form interfacial charge transfer (CT) excitons or exciplex states.^[28,30] Once the excitons or exciplex states recombine, the energy relaxed from the recombination is possibly transferred to the proximal holes (electrons) through an Auger process, and the holes (electrons) that have gained sufficient energy will be injected into the other side to recombine with the electrons (holes), respectively. Therefore, the required turn-on voltage is smaller than the bandgap voltage. When the bias is large enough that the electrons/holes gain enough energy to overcome the barrier, the direct injection then dominates the charge transfer process.

The luminance–current relation is a good indicator for revealing the charge injection dynamics. The current yield is

plotted versus the applying bias, as shown in Figure 3D,E. Here the current yield is defined by the EL peak intensity divided by the current density (current yield = EL peak/current density). As can be seen from Figure 3D, in the low voltage regime, the red emission peak intensity increases superlinearly with the current density, while in the voltage regime above the bandgap voltage, there is an approximately linear relationship between the luminance and the current density. As the Auger process requires three carriers, the result suggests that the Auger-assisted charge up-conversion process is made responsible for the sub-bandgap turn-on voltage. However, for the green emission (Figure 3E), the superlinear region extends to a high voltage of 3.3 V, which is larger than the energy bandgap of CsPbBr₃. In addition to the Auger process, the saturation of nonradiative defects with increasing carrier density, which results from the increase of the applying voltage, may also contribute to the superlinear relationship of the luminance–current in the low bias regime. Apparently, for the green emission at the voltage larger than the value related to the energy bandgap of CsPbBr₃, the carrier saturation effect may play an important role in the super-linear behavior of the luminance versus current.

The emission color with respect to the applied voltage can be controlled by the structure engineering (Figure 3F). The turning-point voltage corresponding to the equal intensity of red and green emission moves to a high value when a PVP layer is introduced at the NiMgO_x/CsPbBr₃ interface, and increases

to an even higher value when an additional poly(methyl methacrylate) (PMMA) layer is introduced at the CdSe/ZnMgO interface. The change of the turning-point voltage may be ascribed to the redistribution of the carriers when an interface layer is used. This hypothesis is based on two factors: first, the number of injected electrons is larger than that of injected holes due to the imbalanced energy barrier. Second, hole prefers to inject into CdSe to recombine with electron at low bias region. This is true as the red emission is first observed during the increasing of the applying voltage. So, when a PVP interlayer is inserted between the HTL and CsPbBr₃, at the same voltage, the number of holes left inside CsPbBr₃ is reduced and therefore the green emission decreases. When a PMMA layer is further introduced between ETL/CdSe, the number of the electrons supplying to the active layer is reduced due to the PMMA barrier. Because of the dominated recombination process taking places in CdSe at low bias region, the electrons injected into CsPbBr₃ is reduced, resulting in a decrease of green emission. The rational control of the device structure, therefore, provides a fine adjustment of the electroluminescence. Of interest is that, although the turning-point voltage can vary with different structures, the turn-on voltages of all devices are very similar. The onset of light emission for these devices is all ≈ 1.8 V. This further confirms the Auger-assisted charge transfer process occurring at the CsPbBr₃/CdSe interface.

As shown in Figure 4A,B, the heterojunction device exhibits a high maximum brightness of over $21\,900\text{ cd m}^{-2}$, a peak current efficiency of 13.4 cd A^{-1} , and an external quantum efficiency of 7.5% at 274 cd m^{-2} with bias of 2.42 V. However, the counterpart with a CsPbBr₃ single active layer fabricated under the same conditions and structure exhibits a weak luminance of 100 cd m^{-2} and a low external quantum efficiency of 0.1% (Figure S5, Supporting Information). The significant improvement in the performance can be ascribed to the following facts: 1) As discussed above, the separation of the CsPbBr₃ from the ZnMgO can prevent the accumulation of the carriers that lead to defect-related significant nonradiative recombination, owing to the fact that, as has been reported, the CdSe/Zn(Mg)O interface facilitates the interfacial charge transfer processes.^[26] Furthermore, the charge transfer at the CsPbBr₃/CdSe interface is a benign process, as both active layers have long carrier lifetimes. 2) The heterojunction separates the electrons (in CdSe)

from the holes (in CsPbBr₃) during their transport. The spatial confinement of electrons and holes helps to reduce the nonradiative recombination. 3) In the CsPbBr₃ single-layer device, the recombination zone is close to the HTL/CsPbBr₃ interface due to the imbalanced holes and electrons injection barrier.^[31] However, in the heterojunction device, the electroluminescence recombination zone is controlled so as to keep it away from the HTL/CsPbBr₃ and CdSe/ETL interfaces. This is because the electrons and holes are separated and spatially confined in the CdSe and CsPbBr₃ respectively, at the beginning. Then, they have to overcome the barrier and inject into the opposite side. The carriers that diffuse across the interface become minority carriers in the other side; they then recombine with majority carriers, dying out with distance (Figure S6, Supporting Information). As the injected minority carriers accumulate at the CsPbBr₃/CdSe interface, the main recombination zone is kept away from the HTL/CsPbBr₃ and the CdSe/ETL interfaces.

In addition to the good performance, the heterojunction device demonstrates constant light emission during multiple measurement and superior stability when exposed to the ambient conditions. Figure S7 (Supporting Information) shows the electroluminescence intensity variation of the green (520 nm) and red emission (628 nm) measured at a current density of 100 mA cm^{-2} . The heterojunction device shows a significant performance enhancement after 2 days' exposure to the ambient condition, and still exhibits bright electroluminescence after 1080 hours (insets of Figure S7, Supporting Information), with the degradation of 27% and 12% for the green and red emission, respectively. In comparison, the emission of the CsPbBr₃ single-layer device decays rapidly after several rounds of measurement. The poor stability of the CsPbBr₃ device was reported to be the reason of the ion migration, including the electrical induced ion migration and intrinsic ion migration due to the low activation energy for the halide ions.^[32–34] For the LED under positive bias, high electrical field causes severe ionic migration towards the ZnMgO ETL, inducing charge accumulation at the interface and thus the exciton quenching. When CdSe is introduced between the CsPbBr₃ and ZnMgO, it can act as a blocking layer to retard the ionic migration and mitigate the charge accumulation. In addition, it can also passivate the surface of CsPbBr₃ to reduce the trap states. The improvement of the heterojunction device stability may arise from the

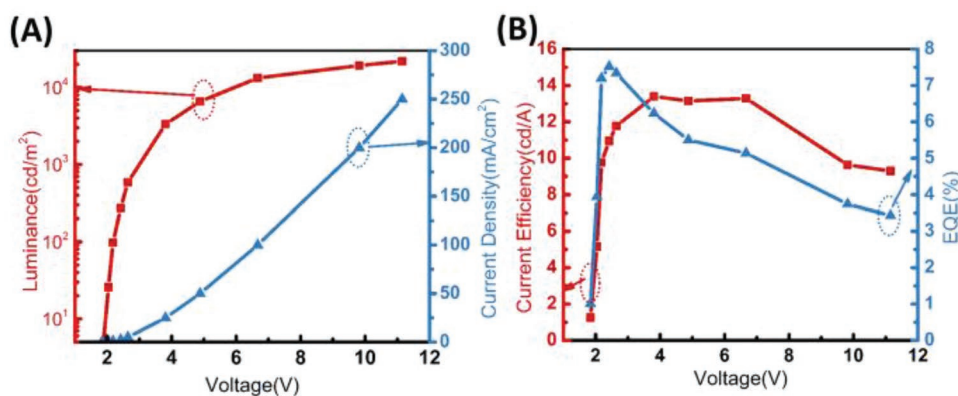


Figure 4. A) Luminance and current density at different applied voltages; B) current efficiency and external quantum efficiency (EQE) at different applied voltages.

retardation of the diffusion of ions/molecules within CsPbBr₃ by the introduction of CdSe, and of course, the control of the recombination zone away from the interfaces and the use of inorganic charge injection layers.

2.3. Light Harvesting and Light Detection

In addition to multicolor LEDs, the heterojunction device can operate as a light-harvesting/detection unit (Figure 5A). As shown in Figure 5B, under the AM1.5 illumination, the device exhibits an extremely high open-circuit voltage (V_{oc}) of 1.73 V. As a comparison, the CsPbBr₃ single-layer device has a V_{oc} of only 1.40 V. Since the built-in potential between the p-type NiMgO and the n-type ZnMgO is only 1.9 eV, the high V_{oc} represents a very low loss-in potential of only 150 mV. It is worth remembering that the low loss-in-potential can be ascribed to the low leakage current, which results from the separation of the CsPbBr₃ from the ZnMgO, as well as the efficient and benign ET process within the CsPbBr₃/CdSe active layer. The low fill factor (FF) may be related to the energy band mismatch between the CdSe and the ZnMgO (Figure 5A). The barrier between them retards the electron transport. This is confirmed by the FF improvement when an ultrathin phenyl-C₆₁-butyric acid methyl ester layer (PCBM, ≈20 nm) is introduced at the interface of the CdSe/ZnMgO to promote the electron injection. The device with a PCBM layer exhibits a V_{oc} of 1.69 V, a short-circuit current (J_{sc}) of 3.4 mA cm⁻², an

a FF of 0.72, and thus a power conversion efficiency (PCE) of 4.2%. Although the device is not among the highest efficiencies reported for the CsPbBr₃-based solar cells, the result is extremely encouraging considering the ultrathin thickness of the absorbing layer (110–120 nm) and the electrical properties, such as the V_{oc} and FF, are high enough for such wide bandgap solar cells. The high V_{oc} and FF, in turn, suggest an efficient charge separation and collection process in the heterojunction device.

Figure 5C shows the photosensitivity at different biases, characterized by means of the light/dark current ratio, with an incident white light intensity of 0.8 mW cm⁻². Compared with the CsPbBr₃ single-layer device, the heterojunction device exhibits higher photosensitivity in both photoconductive mode (reverse bias region) and photovoltaic mode (positive bias region). Particularly, near the zero bias, the on/off ratio can be as high as 10⁴–10⁵. Additionally, built-in voltage is extremely high, which is in good agreement with the result of J - V measurement under 1-sunlight intensity. It is interesting to note that, unlike the CsPbBr₃ single-layer device, the heterojunction device also shows photosensitivity at a bias region between 1.5 and 2.1 V. As an example, the photoresponse of the device operated at the bias of 1.8 V is given in Figure S8 (Supporting Information). And in this bias region, the device can also emit light (Figure S8, Supporting Information), which means that the heterojunction device could act as an LED and a photosensor simultaneously. However, in this regime, both of the LED and photosensor are inefficient, which limits their practical applications.

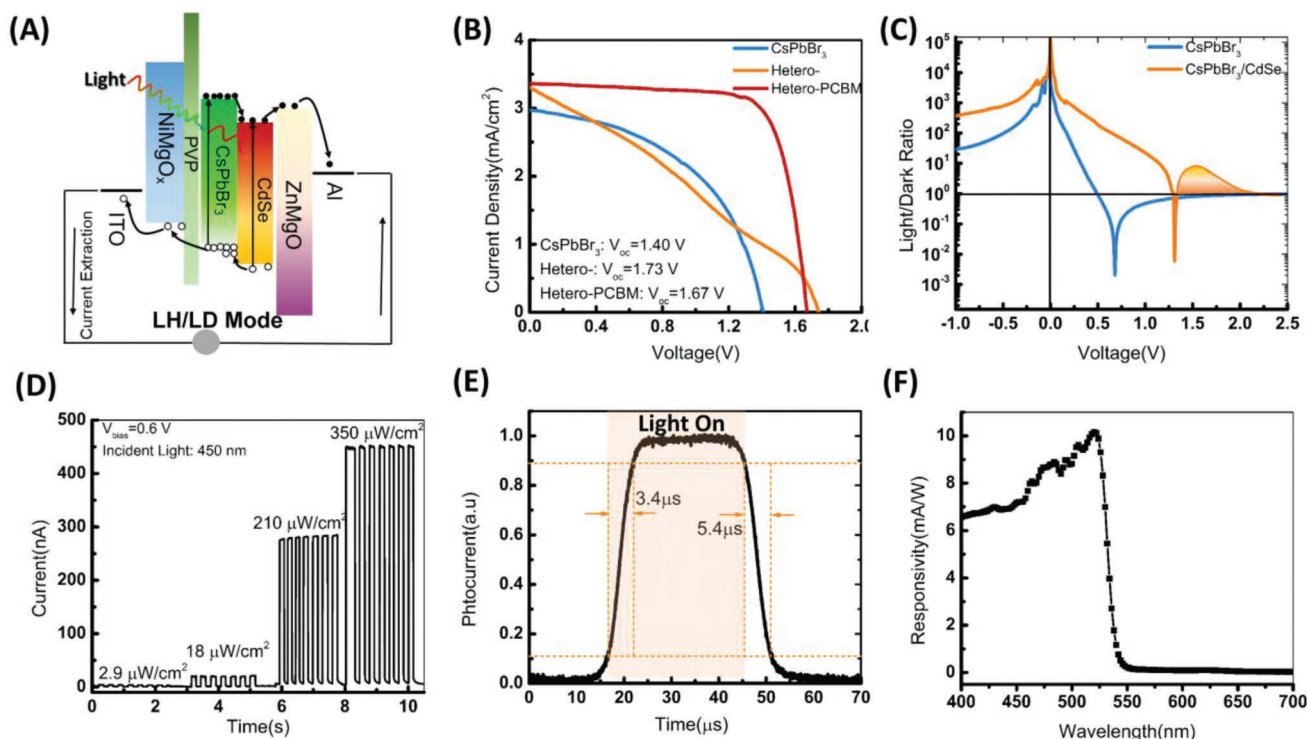


Figure 5. A) The schematic of the device operation at a light-harvesting (LH)/light detection (LD) mode; B) J - V curve of the devices with active layers and structures; C) light/dark current ratio for the CsPbBr₃ single-layer device and the heterojunction devices. The incident white light intensity is 0.8 mW cm⁻²; D) photoresponse to different light intensities; E) Photocurrent in response to illumination by a blue LED source (400 nm) driven by a chopper. Response time is defined as the time between 10% and 90% of the maximum photocurrent; F) the responsivity of the device under a bias of -0.5 V.

The temporal photoresponse of the heterojunction device was measured under illumination at 450 nm. The light intensity was attenuated by different neutral filters (Figure 5D). The device can detect extremely weak light up to $2.9 \mu\text{W cm}^{-2}$, exhibits good on-off switching, and preserves over multiple cycles, all of which indicate the robustness and credibility of our photodetector. The response speed was investigated under a 405 nm pulsed light from an LED. From the transient photocurrent response (Figure 5E), the rise and fall times are calculated to be 3.4 and 5.4 μs , respectively. The ultrafast response is as a result of the high electrical field and the ultrafast charge separation by the type II heterojunction structure. The responsivity of the device to different input light wavelengths was measured and is shown in Figure 5F. The device exhibits a responsivity of 6–10 mA W^{-1} below 525 nm wavelength light. At the wavelength of $\approx 550\text{--}650$ nm, the device also has a weak photoelectric response due to the absorption of the CdSe (Figure S9, Supporting Information), suggesting the CdSe acts as the active layer instead of the functional interfacial layer in the device.

3. Conclusion

Unlike the previously conceived heterojunction that is widely formed between the charge transport layers and the active layer, the heterojunction demonstrated here is inside the active layer. This double active layer can not only provide a path for charge separation or exciton dissociation in an efficient and benign process, but also enhances the charge injection and recombination due to the following facts: 1) Spatially confining electrons and holes in separated active layers to suppress the nonradiative recombination; 2) Separating the CsPbBr_3 from the ZnMgO to prevent the accumulation of the carriers that lead to defect-related significant nonradiative recombination; 3) Controlling the recombination zone away from the interfaces; 4) providing barriers for the accumulation of the electrons and holes within the active layer to promote the Auger-assisted charge injection process.

In summary, with the heterojunction active layer, we have demonstrated that the individual device can serve as a voltage controllable multicolor LED, an efficient solar cell, and a sensitive photodetector, which results from the anisotropic properties of the heterojunction active layer. The combination of one or two functions of them will lead to versatile applications. For example, the voltage controllable multicolor electroluminescence property can be used to make field sequential displays and smart lighting. The emission and detection at different operation modes and different position can be employed to build on-chip optical interconnect. The proper design of light emission and light harvesting can find place in an ecofriendly applications.

Compared with the single-active-layer device, the heterojunction device exhibits key features of merit, including bright and stable electroluminescence, exceptionally high photovoltage, good and ultrafast on-off switching. Furthermore, the heterojunction device has simultaneous optical signal detection and light emission. These features of merit open up new approaches to future advanced applications.

4. Experimental Section

Materials: PbBr_2 , CsBr was purchased from Sigma Aldrich, AVABr was purchased from GreatCell Solar, [6,6]-phenyl-C61-butyric acidmethyl ester (PCBM) was purchased from Lumtec. CdSe QDs and ZnMgO nanoparticles were purchased from Poly Optoelectronics.

Device Fabrication: The ITO substrate was first patterned by laser scribing, and then cleaned with a detergent solution and rinsed. UV-ozone treatment was conducted prior to the sputtering, and a 35 nm NiMgO_x layer was then sputtered onto the cleaned ITO substrate, followed by a postannealing. The details of the NiMgO_x growth procedure are described elsewhere.^[18] If necessary, a 0.5 wt% PVP solution in DMSO was spin-coated onto the NiMgO_x prior to the CsPbBr_3 deposition and then annealed at 150 °C for 10 min. The AVABr-doped CsPbBr_3 was prepared from a precursor solution containing 0.5 M PbBr_2 (99%, Sigma-Aldrich), 1.1 M CsBr (99.9%, Sigma-Aldrich), 0.05 M AVABr in 1 mL anhydrous DMSO:GBL (9:1, v/v). After a vigorous stirring at 45 °C for overnight, top transparent solution was decanted and filtered for using.^[24] The perovskite solution was then spin coated onto the PVP at 800 rpm for 5 s and 3000 rpm for 30 s. After the spin coating, the substrate was immediately put on a hot plate preheated to 100 °C for 5 min. Then the CdSe QDs were spin coated onto the CsPbBr_3 from a 20 mg mL^{-1} solution in octane. After the drying of the CdSe QDs at 100 °C for 5 min, ZnMgO (30 mg mL^{-1} in ethanol) was spin coated at 3000 rpm to serve as the electron injection layer. Finally, the device was completed by thermal evaporation of a 100 nm Al cathode. The device area was defined to be 4 mm^2 .

Characterization: The optical measurements were carried out on an Ocean Optics spectrophotometer. X-ray diffraction patterns were measured using an X-ray diffractometer (Panalytical X'Pert Pro), using $\text{Cu K}\alpha$ radiation ($\lambda = 1.54050 \text{ \AA}$). SEM images were obtained using an analytical field emission SEM (JEOL-7100F). Steady PL measurement was conducted with a home-made system, for which an LED of 405 nm was used as the excitation light source and PR650 was used as the spectrophotometer. TRPL were carried out by an Edinburgh Instruments F1000. The excitation light has a wavelength of 358 nm. UPS measurements were conducted on a Kratos Axis Ultra DLD multitechnique surface analysis system using HeI (21.22 eV) radiation.

Current-voltage characteristics were measured under simulated AM1.5G sunlight at 100 mW cm^{-2} irradiance, generated by a 450W xenon lamp (Oriel, Sol2A) light source. The light intensity was calibrated using an NREL calibrated Si reference cell. Dark and light current-voltage was measured using an IV probe station equipped with a white light. The electroluminescence spectra were obtained with a PR-650 spectrometer and a Keithley 2400 power source. Constant current was applied to the device during the measurement. The photodetector performance was characterized using a home-built system consisting of two multiplexers, a preamplifier, a laptop computer, and the Labview program. The transient photoresponse was measured under 400 nm pulsed excitation. The responsivity of the device at different wavelength was measured with the home-built system, the incident light with different wavelengths were realized by the Edinburgh Instruments F1000 system.

Supporting Information

Supporting Information is available from the Wiley Online Library or from the author.

Acknowledgements

This work was financially supported by the National Natural Science Foundation of China (61804097), Natural Science Foundation of Guangdong Province, China (2018A030310596), the Science and Technology Innovation Commission of Shenzhen (JCYJ20170818095753613), Natural Science Foundation of SZU

(Grant No. 2017008), Principal Fund of SZU (Grant No. 85704-000002), the Science and Technology Innovation Commission of Shenzhen (Grant No. ZDSYS201707271554071), and the funding from State Key Laboratory of Advanced Displays and Optoelectronics Technologies (HKUST). The authors acknowledge Nano system Fabrication Facility (NFF) of HKUST for the device/system fabrication and Materials Characterization and Preparation Facility (MCPF) of HKUST for the characterization.

Conflict of Interest

The authors declare no conflict of interest.

Keywords

asymmetric active layer, heterojunction, multicolor electroluminescence, multifunctional optoelectronic device, perovskite

Received: November 6, 2018

Revised: January 13, 2019

Published online:

-
- [1] R. W. Keyes, *Rep. Prog. Phys.* **2005**, *68*, 2701.
- [2] Y.-Q. Bie, G. Grosso, M. Heuck, M. M. Furchi, Y. Cao, J. Zheng, D. Bunandar, E. Navarro-Moratalla, L. Zhou, D. K. Efetov, T. Taniguchi, K. Watanabe, J. Kong, D. Englund, P. Jarillo-Herrero, *Nat. Nanotechnol.* **2017**, *12*, 1124.
- [3] C. Liu, Y. Cai, H. Jiang, K. M. Lau, *Opt. Lett.* **2018**, *43*, 3401.
- [4] K. H. Li, W. Y. Fu, Y. F. Cheung, K. K. Y. Wong, Y. Wang, K. M. Lau, H. W. Choi, *Optica* **2018**, *5*, 564.
- [5] C.-J. Yang, T.-Y. Cho, C.-L. Lin, C.-C. Wu, *Appl. Phys. Lett.* **2007**, *90*, 173507.
- [6] M. Guan, L. Li, G. Cao, Y. Zhang, B. Wang, X. Chu, Z. Zhu, Y. Zeng, *Org. Electron.* **2011**, *12*, 2090.
- [7] U. Vogel, P. Wartenberg, B. Richter, S. Brenner, M. Thomschke, K. Fehse, J. Baumgarten, *SID Symp. Dig. Tech. Pap.* **2015**, *46*, 66.
- [8] G. Li, K. L. Ching, J. Y. L. Ho, M. Wong, H.-S. Kwok, *Adv. Energy Mater.* **2015**, *5*, 1401775.
- [9] M. A. Green, A. Ho-Baillie, H. J. Snaith, *Nat. Photonics* **2014**, *8*, 506.
- [10] G. Li, H. Li, J. Y. L. Ho, M. Wong, H. S. Kwok, *Nano Lett.* **2014**, *14*, 2563.
- [11] H. Y. Chen, W. Y. Lam, J. D. Luo, Y. L. Ho, B. Z. Tang, D. B. Zhu, M. Wong, H. S. Kwok, *Appl. Phys. Lett.* **2002**, *81*, 574.
- [12] N. Oh, S. Nam, Y. Zhai, K. Deshpande, P. Trefonas, M. Shim, *Nat. Commun.* **2014**, *5*, 3642.
- [13] N. Oh, B. H. Kim, S.-Y. Cho, S. Nam, S. P. Rogers, Y. Jiang, J. C. Flanagan, Y. Zhai, J.-H. Kim, J. Lee, Y. Yu, Y. K. Cho, G. Hur, J. Zhang, P. Trefonas, J. A. Rogers, M. Shim, *Science* **2017**, *355*, 616.
- [14] H. Zhang, X. Sun, S. Chen, *Adv. Funct. Mater.* **2017**, *27*, 1700610.
- [15] X. Peng, L. Manna, W. Yang, J. Wickham, E. Scher, A. Kadavanich, A. P. Alivisatos, *Nature* **2000**, *404*, 59.
- [16] F. Deschler, M. Price, S. Pathak, L. E. Klintberg, D.-D. Jarausch, R. Higler, S. Hüttner, T. Leijtens, S. D. Stranks, H. J. Snaith, M. Atatüre, R. T. Phillips, R. H. Friend, *J. Phys. Chem. Lett.* **2014**, *5*, 1421.
- [17] L. Protesescu, S. Yakunin, M. I. Bodnarchuk, F. Krieg, R. Caputo, C. H. Hendon, R. X. Yang, A. Walsh, M. V. Kovalenko, *Nano Lett.* **2015**, *15*, 3692.
- [18] G. Li, Y. Jiang, S. Deng, A. Tam, P. Xu, M. Wong, H.-S. Kwok, *Adv. Sci.* **2017**, *4*, 1700463.
- [19] G. Li, S. Deng, M. Zhang, R. Chen, P. Xu, M. Wong, H.-S. Kwok, *Sol. RRL* **2018**, *2*, 1800151.
- [20] H. McDaniel, P. E. Heil, C.-L. Tsai, K. (Kevin) Kim, M. Shim, *ACS Nano* **2011**, *5*, 7677.
- [21] S. Kumar, M. Jones, S. S. Lo, G. D. Scholes, *Small* **2007**, *3*, 1633.
- [22] V. I. Klimov, S. A. Ivanov, J. Nanda, M. Achermann, I. Bezel, J. A. McGuire, A. Piryatinski, *Nature* **2007**, *447*, 441.
- [23] S. Suckow, T. M. Pletzer, H. Kurz, *Prog. Photovoltaics* **2014**, *22*, 494.
- [24] L. Zhang, X. Yang, Q. Jiang, P. Wang, Z. Yin, X. Zhang, H. Tan, Y. (Michael) Yang, M. Wei, B. R. Sutherland, E. H. Sargent, J. You, *Nat. Commun.* **2017**, *8*, 15640.
- [25] C. Liu, W. Li, C. Zhang, Y. Ma, J. Fan, Y. Mai, *J. Am. Chem. Soc.* **2018**, *140*, 3825.
- [26] B. S. Mashford, M. Stevenson, Z. Popovic, C. Hamilton, Z. Zhou, C. Breen, J. Steckel, V. Bulovic, M. Bawendi, S. Coe-Sullivan, P. T. Kazlas, *Nat. Photonics* **2013**, *7*, 407.
- [27] A. Brumberg, B. T. Diroll, G. Nedelcu, M. E. Sykes, Y. Liu, S. M. Harvey, M. R. Wasielewski, M. V. Kovalenko, R. D. Schaller, *Nano Lett.* **2018**, *18*, 4771.
- [28] W. Ji, P. Jing, L. Zhang, D. Li, Q. Zeng, S. Qu, J. Zhao, *Sci. Rep.* **2015**, *4*, 6974.
- [29] L. Qian, Y. Zheng, K. R. Choudhury, D. Bera, F. So, J. Xue, P. H. Holloway, *Nano Today* **2010**, *5*, 384.
- [30] R. S. Sanchez, M. S. de la Fuente, I. Suarez, G. Munoz-Matutano, J. P. Martinez-Pastor, I. Mora-Sero, *Sci. Adv.* **2016**, *2*, e1501104.
- [31] A. Sadhanala, A. Kumar, S. Pathak, A. Rao, U. Steiner, N. C. Greenham, H. J. Snaith, R. H. Friend, *Adv. Electron. Mater.* **2015**, *1*, 1500008.
- [32] P. Calado, A. M. Telford, D. Bryant, X. Li, J. Nelson, B. C. O'Regan, P. R. F. Barnes, *Nat. Commun.* **2016**, *7*, 13831.
- [33] C. Eames, J. M. Frost, P. R. F. Barnes, B. C. O'Regan, A. Walsh, M. S. Islam, *Nat. Commun.* **2015**, *6*, 7497.
- [34] P. Vashishtha, J. E. Halpert, *Chem. Mater.* **2017**, *29*, 5965.